Time evolution of temperature profiles retrieved from 13 years of IASI data using an artificial neural network

Marie Bouillon[1], Sarah Safieddine[1], Simon Whitburn[2], Lieven Clarisse[2], Filipe Aires[3], Victor Pellet[3], Olivier Lezeaux[4], Noëlle A. Scott[5], Marie Doutriaux-Boucher[6], Cathy Clerbaux[1,2]

[1]LATMOS/IPSL, Sorbonne Université/UVSQ/CNRS, Paris, France
[2]Spectroscopy, Quantum Chemistry and Atmospheric Remote Sensing (SQUARES), Université Livre de Bruxelles (ULB), Brussels, Belgium
[3]LERMA, Observatoire de Paris/CNRS, Paris, France
[4]SPASCIA, Ramonville-Saint-Agne, France
[5]Laboratoire de Météorologie Dynamique, IPSL/CNRS/Ecole Polytechnique/Université Paris-Saclay, Palaiseau, France
[6]~~European Organisation for the Exploitation of Meteorological Satellites~~EUMETSAT, Darmstadt, Germany

Correspondence to: Marie Bouillon (marie.bouillon@latmos.ipsl.fr)

Abstract. The three Infrared Atmospheric Sounding Interferometers (IASI ~~instruments~~, launched in 2006, 2012, and 2018, are key instruments to weather forecasting, and most meteorological centers assimilate IASI nadir radiance data into atmospheric models to feed their forecasts. The EUropean organisation for the exploitation of METeorological SATellites (EUMETSAT) recently released a reprocessed homogeneous radiance record for the whole IASI observation period, from which thirteen years (2008-2020) of temperature profiles can be obtained. In this work, atmospheric temperatures at different altitudes are retrieved from IASI radiances measured in the carbon dioxide absorption bands (654-800 cm^{-1} and 2250-2400 cm^{-1}) by selecting the channels that are the most sensitive to the temperature at different altitudes. We rely on an Artificial Neural Network (ANN) to retrieve atmospheric temperatures from a selected set of IASI radiances. We trained the ANN with IASI radiances as input and the European Centre for Medium-range Weather Forecasts (ECMWF) reanalysis version 5 (ERA5) as output. The retrieved temperatures were validated with ERA5, with in-situ radiosonde temperatures from the Analysed RadioSoundings Archive (ARSA) network and with EUMETSAT temperatures retrieved from IASI radiances using a different method. Between 750 and 7 hPa, where IASI is most sensitive to temperature, a good agreement is observed between the three datasets: the differences between IASI on one hand, and ERA5, ARSA or EUMETSAT on the other hand are usually less than 0.5 K at these altitudes. At 2 hPa, as the IASI sensitivity decreases, we found differences up to 2 K between IASI and the three validation datasets. We then computed atmospheric temperature linear trends from atmospheric temperatures between 750 and 2 hPa. We found that in the past thirteen years, there is a general warming trend of the troposphere, that is more important at the poles ~~than at the equator~~and at midlatitudes (~~0.7 K/decade at the equator~~0.5 K/decade at mid latitudes, 1 K/decade at the North Pole). The stratosphere is globally cooling on average, except at the South Pole as a result of the ozone layer recovery and a sudden stratospheric warming in 2019. The cooling is most pronounced in the equatorial upper stratosphere (-1 K/decade). This work shows that ANN can be a powerful and simple tool

to retrieve IASI temperatures at different altitudes in the upper troposphere and in the stratosphere, allowing us to construct a
35 homogeneous and consistent temperature data record adapted to trend analysis.

1 Introduction

Atmospheric temperatures are a key component of Earth's climate. In the past few decades, a warming of the troposphere due to the increase of greenhouse gas concentrations (Tett et al., 2002; Santer et al., 2017; Susskind et al., 2019; Shanbaum et al., 2014) and a cooling of the stratosphere have been observed (Randel et al., 2016; Maycock et al., 2018). Stratospheric
40 temperatures are impacted by both anthropogenic forcing (e.g. greenhouse gas emissions, ozone depletion) and natural forcing (e.g. volcanic eruptions, solar cycle) (Aquila et al., 2016). The study of stratospheric temperatures and their long-term evolution is therefore critical to understand the roles of these different forcings on the evolution of climate in the stratosphere, but also in the troposphere.

45 Long-term atmospheric temperature records can be ~~are~~ obtained from in situ measurements (lidars and radio soundings). These observations are generally of excellent quality, however, they are sparse and unevenly distributed around the globe. More recently, satellite-derived temperatures have become a key component for climate change monitoring (Li et al., 2011; Yang et al., 2013). Satellite observations have a better spatial coverage but the construction of a long temperature record from these observations usually requires merging several different instruments, and corrections and adjustments between the
50 observations are needed to obtain a homogeneous dataset (Zou et al., 2014; Seidel et al., 2016).

In 2006, the first Infrared Atmospheric Sounding Interferometer (IASI) was launched on the Metop satellite. IASI measures radiance spectra from which surface and atmospheric temperatures (Hilton et al., 2012; Safieddine et al., 2020a) and trace gas concentrations can be retrieved (Clerbaux et al., 2009; Clarisse et al., 2011). A second instrument and then a third ~~and a~~
55 ~~third instruments~~ were launched in 2012 and 2018, and the comparison between the three instruments have shown excellent agreement (Boynard et al., 2018; EUMETSAT, 2013a). Since IASI is planned to fly for at least 18 years, with the three instruments built at the same time and flying in constellation, continuity and stability are e~~i~~nsured, and the construction of a long-term climate data record ~~the potential of constructing a long-term climate data record~~ at a range of altitudes is becoming possible~~evident~~.

60

IASI radiance spectra and derived atmospheric temperature profiles are routinely processed by the European organisation for the exploitation of METeorological SATellites (EUMETSAT). Over the past 13 years, EUMETSAT has performed several updates on the real time processing of both radiances and temperatures, making the time series non-homogeneous. The impacts of these updates have been evidenced in several studies (George et al., 2015; Van Damme et al., 2017; Parracho et
65 al., 2021) and quantified in Bouillon et al. (2020). For temperatures, the "jumps" in the time series due to these updates make

them unfit for the computation of trends. In 2018, EUMETSAT reprocessed Metop-A radiance dataset (doi:10.15770/EUM_SEC_CLM_0014) , providing a new radiance dataset over time. After 2018, the radiances are stable and consistent with those reprocessed (Bouillon et al., 2020).

In this work, we present a new atmospheric temperature product derived from the homogeneous IASI radiance dataset, using an Artificial Neural Network (ANN) technique, in order to derive a homogeneous temperature data record. In Sect. 2, we present the data used in this study and in Sect. 3, we explain the method used to compute the temperatures, both the selection of IASI channels and the training of the ANN. In Sect. 34, we compare the outputs of the neural network with both the latest ECMWF reanalysis (ERA5) and ARSA radiosondes temperatures to validate the new data. In Sect. 54 we compute atmospheric temperature trends for the past 13 years. Conclusions are listed in Sect. 65.

2 Data

2.1 IASI radiances

Each of the three IASI instruments are mounted on-board the Metop platform flying on a polar orbit at an altitude of 817 km. The IASI swath contains 30 fields of view with 4 pixels in each field of view. This observation mode allows each IASI instrument to observe the entire Earth twice a day, between 9:15 and 9:45 AM and PM local time. IASI measures the radiation of the Earth-atmosphere system in the thermal infrared in 8461 channels between 645 and 2760 cm^{-1} (resolution of 0.25 cm^{-1}, 0.5 cm^{-1} apodized; Clerbaux et al., 2009).

2.2 ERA5 reanalysis

The European Center for Medium-range Weather Forecast (ECMWF) reanalysis, ERA5 (Hersbach et al. 2018, Copernicus Climate Change Services) is a 4D-Var data assimilation product. It is part of the Integrated Forecast System (IFS) that provides variables relevant to the atmosphere, land and ocean. ERA5 atmospheric temperature product used in this work is hourly, and is available on 37 pressure levels (from the surface up to 0.01 hPa). ERA5 actually assimilates IASI radiances from Metop-A and Metop-B, as well as high spectral resolution radiances from other instruments such as the Atmospheric InfraRed Sounder (AIRS) on Aqua, and the Cross-track Infrared Sensor from the Suomi National Polar-orbiting Partnership and the National Oceanic and Atmospheric Administration-20. Note that IASI is the largest contributor to error reduction for global numerical weather prediction in the thermal infrared spectral band (Borman et al., 2016).

2.3 Analysed RadioSoundings Archive

The Analysed RadioSoundings Archive (ARSA) is a 41-year (1979-2019) database of radiosonde temperature profiles measurements from different stations around the globe (Scott et al., 2015). ARSA provides 43 pressure-level profiles (from the surface to 0.0026 hPa) of temperature, water vapour and ozone, and surface temperature. The raw radiosonde

observations go through severe multistep quality controls, to eliminate gross errors. If the selected radiosonde measurement is unable to provide forward radiative transfer modelers with the required information (above 30 hPa for temperature), ARSA combines existing radiosonde measurements with other reliable data sources to complete the description of the atmospheric state as high 0.0026 hPa. Temperature profiles are thus extrapolated with ERA-Interim (Dee et al., 2011) outputs between 30 hPa and 0.1 hPa for temperature. Above 0.1 hPa, the profiles are extrapolated up to 0.0026 hPa using a climatology of ACE (Atmospheric Chemistry Experiment)/Scisat Level 2 temperature products. ARSA was validated against IASI observations by simulating spectra from the Automatized Atmospheric Absorption Atlas (4A/OP) forward model (Scott and Chédin, 1981) with ARSA profiles as inputs, and comparing them with space-time colocated IASI observations. The pertinence of the requested modifications after this validation has been also assessed against the TIROS Operational Vertical Sounder (TOVS), the Advance TIROS Operational Vertical Sounder (ATOVS, Reale et al., 2008), AIRS (Lambrigtsen et al., 2004), the High resolution Infrared Radiation Sounder (HIRS4, EUMETSAT, 2013b), and the Microwave Humidity Sounder (MHS, Hans et al., 2020). Based on these validations, incorrect or unreliable data inherent to the quality of the radiosondes were completed other relevant auxiliary datasets (in particular Level 2 results of ACE-FTS temperature profiles above 10 hPa) measurement data. It is useful to recall that ARSA is being reprocessed to replace ERA-Interim with ERA5. This will allow, among other things, to extend the period beyond summer 2019, when the production of ERA-Interim stopped.

2.4 EUMETSAT CDR of all-sky temperature profiles

In 2020, EUMETSAT released a climate data record (CDR) of all-sky IASI temperature (doi:10.15770/EUM_SEC_CLM_0027), so the temperature is homogeneous over the whole IASI time series (EUMETSAT, 2020). The reprocessed temperatures were computed with a Piece-Wise Linear Regression Cube (PWLR[3]) algorithm, using all IASI observations in input (clear and cloudy scenes), and observations from two other microwave instruments flying onboard the Metop-A and -B satellites: the Microwave Humidity Sounding (MHS) and the Advanced Microwave Sounding Unit (AMSU-A).

The basic principle of this algorithm is a linear regression between IASI radiance observations and real atmospheric temperatures. To take into account the non-linearity between the observations and the temperatures, the training dataset is divided into several sub-datasets, resulting from a k-mean clustering. This ensure that, in each sub-dataset, a linear relationship is a good approximation between the observations and the temperature and different linear regression coefficients are computed for each sub-dataset.

3̶2 Methods

3̶2.1 The IASI instrument channel selection

~~Each of the three IASI instruments are mounted on-board the Metop platform flying on a polar orbit at an altitude of 817 km. The IASI swath contains 30 fields of view with 4 pixels in each field of view. This observation mode allows each IASI instrument to observe the entire Earth twice a day, between 9:15 and 9:45 AM and PM local time. IASI measures the radiation of the Earth-atmosphere system in the thermal infrared in 8461 channels between 645 and 2760 cm^{-1} (resolution of 0.25 cm^{-1}, 0.5 cm^{-1} apodized; Clerbaux et al., 2009).~~

Using the 8461 channels of IASI raises practical issues for storage and computation power, as retrieval and assimilation algorithms can hardly handle such a large amount of information. A channel selection is usually needed when dealing with IASI (Rabier et al., 2002; Collard, 2007; Pellet and Aires, 2018). To retrieve atmospheric temperatures, we select IASI channels that are most sensitive to the temperature profile. Most of the channels selected are located in the carbon dioxide (CO_2) absorption band, because the radiances observed in these channels are more sensitive to atmospheric temperature~~is mostly impacted by atmospheric temperatures, rather~~ than CO_2 concentrations (Chédin et al., 2003; Collard, 2007). The selection is obtained using the Entropy Reduction (ER) method (Rodgers, 2000). The entropy describes the probabilities of all the possible states and it is maximal when all the states have an equal probability. Selecting the channels that reduce the most the entropy means selecting the channels that bring the most information about the state. ER is computed using:

$$ER = \frac{1}{2}\log_2(\mathbf{BA^{-1}}) \tag{1}$$

where $\mathbf{B}$ is the a priori covariance matrix and $\mathbf{A}$ is the retrieval covariance matrix, described in the following Eq. 2:

$$\mathbf{A = (B^{-1} + H^T R^{-1} H)^{-1}}, \tag{2}$$

where $\mathbf{H}$ is the matrix of the temperature ~~Jacobians~~ weighting functions (the sensitivity of the IASI brightness temperature to the temperature), and $\mathbf{R}$ is the instrumental noise plus the radiative transfer error.

With $\mathbf{A}$, it is possible to compute the entropy reduction of each channel as such:

$$\boldsymbol{\delta ER} = \frac{1}{2}\log_2\big(1 + \mathbf{h'^T A_{i-1} h'}\big), \tag{3}$$

with $\mathbf{h}$' being the Jacobian of the considered channel normalized by the noise ($\mathbf{H}$' = $\mathbf{R}^{-1/2}\mathbf{H}$). For the selection of the first channel, we set $\mathbf{A_0}$=$\mathbf{B}$. With this, we selected the channel with the largest entropy reduction, and the theoretical covariance matrix is updated as follows:

$$A_i = A_{i-1} - \frac{(A_{i-1}h')(A_{i-1}h')^T}{1+ (A_{i-1}h')^T h'} \ . \tag{4}$$

We then repeat this process until the chosen number of channels have been selected or until the entropy has been reduced enough. This method has been used to retrieve land surface~~skin~~ temperature from IASI (Safieddine et al., 2020a), and we apply it here for atmospheric temperature profiles.

155

~~In order t~~To take into account the effect of the different parameters affecting the selection, two experiments were made: in the first, we considered 200 channels. The channels were selected while taking into account the perturbation of the radiances due to water vapour (H_2O) and ozone (O_3) variations because some channels are sensitive to temperature, H_2O and O_3 (Pellet and Aires, 2018). The uncertainty on the state of unretrieved species (i.e H_2O and O_3) impacts the potential retrieval of the

160 temperature using these channels. This perturbation is then computed with $H_x \times B_x \times H_x^T$ (with x being the variable considered: H_2O or O_3) and is added to the instrumental noise and radiative transfer error, so A becomes:

$$A = \left\{ B_{temp}^{-1} + H_{temp}^T \left(R + H_{H2O}B_{H2O}H_{H2O}^T + H_{O3}B_{O3}H_{O3}^T \right)^{-1} H_{temp} \right\}^{-1}. \tag{5}$$

The second experiment consists of 100 channels. Before the ER method is applied to all the channels, the channels for which the variability of atmospheric gases (H_2O, O_3, CO and CH_4) and emissivity has an impact higher than 30% of the

165 instrumental noise are removed.

In the first selection, the weighting functions~~Jacobians~~ were computed with the Optimal Spectral Sampling (OSS) radiative transfer model (Moncet et al., 2015). In the second selection, the model used was Radiative Transfer for TOVS (RTTOV, Saunders et al., 2018).

170

For each of the two selection methods, the number of channels selected is increased until adding more new channels does not significantly improves the results.

The goal of using these two sets of experiments is to choose from these two the best and most sensitive channels to different

175 atmospheric temperatures while taking into account the different atmospheric perturbations and errors that might affect the selection. On its own, each experiment was tested (not shown here), and the best result was achieved when combining them both.

For the computation of temperatures, we used a mix of the two experiments, consisting of 231 channels (with 69 channels in

180 common between the two). Figure 1 shows the selected channels on a typical IASI spectrum. Most of the channels are in the ~~v_2~~ carbon dioxide (CO_2) absorption band between 645 and 800 cm^{-1} while few (14 channels) are at 2200 cm^{-1} in ~~v_1~~ the N_2O

absorption band. The full list of the channels is provided in Supplementary material (Table S1).

~~23~~.2 Artificial neural network

We trained a two-layer artificial neural network (ANN) to estimate atmospheric temperature profiles. This method has been
used for instance in Aires et al.~~,~~ (2002~~)~~, using IASI simulated radiances before its launch.

450 000 IASI observations are used to train the ANN. These observations (3000 scenes per month) were selected randomly around the globe between January 2008 and December 2020. This training dataset is composed of day and night, clear and cloudy sky observations mixed together. The input data consists of the pseudo-normalised radiances (multiplied by 10^4, so that their order of magnitude is not too small compared to temperatures) in the selected channels, as well as the scan angle of the observation. ~~A global monthly CO₂~~A monthly value for global CO_2 concentration was also added to take into account the CO_2 variations that affect~~impact~~ the radiance values measured in the selected channels. The CO_2 monthly values come from the NOAA-Earth System Research Laboratories~~ESRL~~ global monitoring dataset (https://gml.noaa.gov/ccgg/trends/). As the expected output of the training of the ANN, we use the ERA5 temperatures interpolated to the latitudes, longitudes, and time of the IASI observations. These temperatures are given on a static pressure level grid. ~~More information on ERA5 temperatures is provided in Sect. 3.~~ We chose ERA5 because it is the most complete homogeneous dataset of temperatures available, allowing us to select observations in any year and any type of sky. A set of 50 000 different observations (selected the same way as the 450 000) is used to assess the quality of the ANN at the end of the training.

The temperatures are computed at 11 fixed pressure levels: 2, 7, 10, 20, 30, 70, 100, 200, 400, 550 and 750 hPa. These were chosen based on the weighting functions~~Jacobians~~ of the 231 selected channels, shown in Figure 2. The ~~Jacobians~~ weighting functions show the sensitivity of IASI channels to the temperature profile in K/K. The weighting functions do not change significantly under day or night conditions and this does not have an impact on the retrieval. We see in Figure 2 that the weighting functions ~~Jacobians~~ peak at different altitudes, in particular for pressures larger than ~~<~~10 hPa suggesting that IASI has a good information content at these altitudes. The pressure levels were chosen based on a tradeoff between having equally distributed levels along the vertical while matching the maxima of the weighting functions ~~Jacobians~~ of the selected channels. The pressure levels are shown in dashed~~otted~~ horizontal lines in Figure 2. At the selected pressure levels, the vertical resolution goes from 5 to 12 km from the lower to the upper troposphere. In the stratosphere, the resolution goes from 12 km in the lower stratosphere to 25 km above 7 hPa. We tried different configurations for the ANN, changing the number of epochs for the training and the number of neurons in the two hidden layers. The configuration giving the best results is 5000 epochs and 150 neurons in the two hidden layers. As a result, we have an ANN with 233 neurons in the input layer (231 radiance values, 1 scan angle and 1 CO_2 value), 150 neurons in each of the two hidden layers, and 11 neurons in the output layer (the 11 pressure levels shown in horizontal lines in Figure 2).

215 We used the trained ANN to retrieve temperatures from all IASI observations between 2008 and 2020. After the temperature profiles are computed, we use a static filter based on ERA5 mean surface pressure between 2008 and 2020 to account for orography (as some high altitude regions do not have temperature at 750 hPa for instance).

34 Results

Atmospheric temperatures between 2008 and 2020 were computed at the 11 pressure levels. We use Metop-A observations
220 until 2017 and Metop-B observations for 2018 onwards. Metop-A satellite is nowwas exploited on a drifting orbit since June 2017, in order to extend its lifetime to the end of 20212022 (EUMETSAT, 2018). We compare the whole IASI time series with the temperatures from ERA5 reanalysis, from ARSAthe Analyzed RadioSoundings Archive (ARSA) and from the EUMETSAT CDR.

43.1 Comparison with ERA5

225 The European Center for Medium Weather Forecast (ECMWF) reanalysis, ERA5 (Hersbach et al. 2018, Copernicus Climate Change Services) is a 4D-Var data assimilation product. It is part of the Integrated Forecast System (IFS) that provides variables relevant to the atmosphere, land and ocean. ERA5 atmospheric temperature product used in this work is hourly, and is available on 37 pressure levels (from the surface up to 0.01 hPa). ERA5 actually assimilates IASI radiances from Metop-A and Metop-B, as well as high spectral resolution radiances from other instruments such as AIRS on Aqua, and CrIs
230 from S-NPP and NOAA-20. We note that IASI is the largest contributor to error reduction for global numerical weather prediction in the thermal infrared spectral band (Borman et al., 2016).
Although the neural network was trained with ERA5, it does not reproduce the same temperatures. The output of the retrieval is mainly governed by the variations of observed radiances, and ERA5 can be used for validation.

235 ERA5 temperatures are given on a 0.25°×0.25° latitude-longitude grid. For the comparison with the IASI ANN output, ERA5 temperatures were interpolated to the time, latitudes and longitudes of IASI observations. We then computed the daily zonal mean of the IASI-based ANN temperatures and ERA5 and looked at the differences between the two datasets. Figure 3 illustrates the zonal mean differences between the ANN retrievals and ERA5 from 2008 to 2020 for the 11 pressure levels considered in this study, and the time-averaged differences.
240

Between 200 hPa and 750 hPa, the differences are less than 0.5 Ksmall at all latitudes (less than 0.5 K). We see slight seasonal variations of the differences at 200, 400 and 550 hPa. At 750 hPa, the seasonal variations are more pronounced and more often negative than at the other pressure levels. Note that due to orography at this pressure level, there is no data over the South Pole, Greenland and in the major mountain ranges.
245

Between 7 hPa and 100 hPa, the differences between the two datasets are ~~much smaller (~~less than 0.5 K~~)~~ at mid latitudes and at the poles. Around the equator (30°S to 30°N), the differences are slightly larger (1 K). ~~The larger differences over the equator can be explained by the high cloud cover in this region, as high water vapour concentrations contaminate the radiances of the whole IASI spectrum (Parracho et al., 2021).~~ Figure 4 shows the monthly mean of the differences between 10°S and 10°N from 100 to 7 hPa, as well as the monthly zonal wind from ERA5 in the same latitude range. Positive differences (ANN temperatures larger than ERA5) are correlated to negative zonal wind and negative differences are correlated to positive zonal wind. This suggests that the neural network overestimates temperatures during the easterly phase of the Quasi-Biennal Oscillation (QBO).

At 2 hPa, the differences range from -2 K to 2 K globally~~are about 2K (variation of positive and negative differences)~~. This is because the IASI channel selection is less sensitive to temperature changes at these pressure levels. In Figure 2, ~~we see that the Jacobians peaking at these pressure levels are large, but there are few of them, compared to other pressure levels, where the Jacobians are smaller, but more numerous.~~we see that the channels peaking at this pressure level have high sensitivity, but there are fewer of them compared to other pressure levels.

~~Averaged over the whole time series and at all latitude, the mean differences between the ANN output and ERA5 are -0.06, 0.11, 0.00, 0.02, 0.01, 0.01, 0.03, 0.07, 0.04, 0.01 and 0.09 K for each pressure level from 2 to 750 hPa, suggesting a small total bias between the two datasets.~~

When taking day and night observations separately (not shown), there is no significant change of the differences.

Since averaging the differences over longitudes makes them smaller, we looked at the daily spatial differences. We gridded the ANN retrievals and ERA5 (interpolated to IASI coordinates) on a 1°×1° latitude-longitude grid and computed the Root Mean Square (RMS) of the daily differences in each of the 1°×1° ~~pixel~~ bin of the grid and at each pressure level. Figure 5~~4~~ shows the RMS of the daily differences for the 2008-2020 period.

At 750 hPa, ~~the~~ RMS values are ~~small~~ about 0.5 K at the equator ~~(about 0.5 K)~~ and larger at higher latitude s (between 1 and 2 K), especially around mountain ranges, where they reach 3 K and can be due to gravity wave activity. Between 550 hPa and 200 hPa, the RMS are of 0.5 K~~small~~ almost everywhere. There are regions (in particular the Antarctica, Greenland and the Himalaya at 550 hPa) where the RMS ~~are larger and they~~ can reach 2 K. Between 100 hPa and 7 hPa, the RMS are small at high latitude (0.5 K) and large at the equator (between 1.5 and 2 K). At 7 and 10 hPa, the band at the equator with larger RMS reaches higher latitudes (about 50°N and S). The large RMS correspond to the high differences seen at the equator in Figure 3. At 2 hPa, the RMS are between 2 and 3 K everywhere, which is ~~coherent~~ consistent with Figure 3.

34.2 Comparison with ARSA

The Analysed RadioSoundings Archive (ARSA) is a 41 year (1979 2019) database of radiosonde temperature profiles measurements from different stations around the globe (Scott et al., 2015). The raw radiosonde observations go through severe multistep quality controls, to eliminate gross errors. Whenever and wherever the selected radiosonde measurement is unable to provide forward radiative transfer modelers with the required information (above 300 hPa for water vapour and above 30 hPa for temperature), ARSA combines existing radiosonde measurements with other reliable data sources to complete the description of the atmospheric state as high 0.0026 hPa. Temperature and water vapour profiles are thus extrapolated with ERA Interim outputs between 30 hPa and 0.1 hPa for temperature and between 300 hPa and 0.1 hPa for water vapour. Above 0.1 hPa, these same profiles are extrapolated up to 0.0026 hPa using a climatology of ACE/Scisat Level 2 temperature products. ARSA was validated against IASI observations by simulating spectra from the 4A/OP forward model (Scott and Chédin, 1981) with ARSA profiles as inputs, and comparing them with space time colocated IASI observations. The pertinence of the requested modifications after this validation has been also assessed against the TIROS Operational Vertical Sounder (TOVS), the Advance TIROS Operational Vertical Sounder (ATOVS, Reale et al., 2008), the Atmospheric InfraRed Sounder (AIRS, Lambrigtsen et al., 2004), the High resolution Infrared Radiation Sounder (HIRS4, EUMETSAT, 2013b), and the Microwave Humidity Sounder (MHS, Hans et al., 2020). Based on these validations, incorrect or unreliable data inherent to the quality of the radiosondes (e.g. water vapour above 300 hPa) or temperature data above 1 hPa were completed with nominal or revisited ECMWF ERA Interim reanalysis (Dee et al., 2011) data (water vapour profiles) or other relevant auxiliary datasets (in particular Level 2 results of ACE FTS temperature profiles above 10 hPa) measurement data. ARSA provides a 43 pressure level profile (from the surface to 0.0026 hPa) of temperature, water vapour and ozone, and surface temperature. It is useful to recall that ARSA is being reprocessed to substitute ERA5 for ERA Interim. This will allow, among other things, to extend the period beyond summer 2019, when the production of ERA Interim stopped.

For the comparison with our IASI retrievals, we interpolated ARSA temperature profiles to the 11 pressure levels of the ANN and we only kept the stations for which there were at least 300 observations per year between 2008 and 2018. Figure 65 shows the positions of these stations.

We then added the 14 stations present in Antarctica and the 6 stations in Greenland to have observations at high latitudes, although these stations have less than 300 observations per year. The stations in Greenland have between 150 and 300 observations per year on average so the time coverage is still satisfactory. However, in Antarctica, the stations have between 10 and 150 observations per year and (only two stations have more than 100 observations per year), so the time coverage is very low.

We divided the stations into 8 distinct regions, and we computed the daily mean temperature of all the observations of each region. We interpolated IASI temperatures to the latitude, longitude and time of each considered station, and we computed the daily mean IASI temperature in each region. We then computed the differences between the two datasets.

315

Figure 76 shows the daily differences between IASI retrievals and ARSA mean regional temperature in the 8 selected regions between 2008 and 2018 and the time averaged difference profiles. We only show differences between 750 and 30 hPa as ARSA data above 30 hPa does not always come from radiosounding measurement but from the extrapolation datasets. At 2 hPa, we see large positive differences of more than 2 K in all the regions, as for ERA5. Between 7 and 100

320   hPa, the differences are small and mostly negative (about 0.5 K). At 200 hPa and below, the differences remain small and negative in the Pacific, Oceania and East Asia. In Greenland, North America and Europe, the differences at these pressure levels are slightly larger and more often positive (about 0.5 K, up to 1 K in North America and Europe) than in the other regions.

325   In Antarctica and, to a lesser extent, the Arabian Peninsula, there are more daily variations of positive and negative differences, and they are a little larger (about 0.7 K in the Arabian Peninsula and 1 K in Antarctica) than in the other regions. This can be because of the low space (few stations) and time coverage (only for Antarctica) in these regions. However, we see the same pattern than in the other regions: large differences at 2 hPa, small differences at 7 hPa and lower, more positive differences in the troposphere.

330

In all the regions, the time averaged differences range from -0.6 K to 0.6 K except in the Arabian Peninsula at 750 hPa where they reach 0.9 K.

Figure S1 shows the differences between ERA5 and ARSA over the same period and in the same regions, with ERA5
335   interpolated to the latitudes, longitudes and time of the ARSA observations. The differences between ERA5 and ARSA are very similar to those between IASI retrievals and ARSA, but slightly smaller (less than 0.3 K between 750 and 7 hPa). Figure S2 shows the differences between IASI and ERA5 temperatures interpolated to the time and locations of ARSA observations. In most regions, the differences are less than 0.5 K. In Antarctica, in Europe (troposphere only) and in the Arabian Peninsula and Oceania (stratosphere only), the differences can reach 1 K.

340

Figure 8 show the standard deviation of the daily differences between IASI-ANN and ARSA temperatures and the correlation between the two datasets in the 8 regions. In most regions, the standard deviation ranges from 0.5 to 1 K, except in the Arabian Peninsula and East Asia where they reach 1.3 K at 750 hPa, and in Antarctica and Europe where they range from 1 to 2 K. The correlations between IASI-ANN and ARSA temperatures show that there is no significant bias between
345   the two datasets.

Figures 3, 5, 7 and 8~~4 and 6~~ show that between 7 and 750 hPa, the IASI ANN product can be considered as~~gives~~ good quality temperatures, very consistent with the temperatures of the ERA5 and ARSA datasets (differences ~~inferior~~ smaller than~~to~~ 1 K at most latitudes, 2 K at the equator). At 2 hPa, the quality of the ANN product decreases, as it was reflected in the lower count of ~~Jacobians~~ weighting functions of IASI (Figure 2). This means that at 2hPa, the temperatures are not accurate enough to follow the long-term evolution of atmospheric temperatures. However, they can still be used to study large variations of temperature (during extreme events for example).

~~Figure S1 shows the differences between ERA5 and ARSA over the same period and in the same regions, with ERA5 interpolated to the latitudes, longitudes and time of the ARSA observations. The differences between ERA5 and ARSA are very similar to those between IASI retrievals and ARSA, but slightly smaller (less than 0.3 K between 750 and 7 hPa, 2 K or more at 2 hPa).~~

~~34~~3.~~3~~2 Comparison with the EUMETSAT reprocessed temperature record

~~In 2020, EUMETSAT reprocessed the IASI temperature record (doi:10.15770/EUM_SEC_CLM_0027), so it is now homogeneous over the whole IASI time series (EUMETSAT, 2020). The reprocessed temperatures were computed with a Piece-Wise Linear Regression Cube (PWLR³) algorithm, using all IASI observations in input (clear and cloudy scenes), and observations from two other microwave instruments flying onboard the Metop A and B satellites: the Microwave Humidity Sounding (MHS) and the Advanced Microwave Sounding Unit (AMSU-A).~~

~~The basic principle of this algorithm is a linear regression between IASI radiance observations and real atmospheric temperatures. To take into account the non linearity between the observations and the temperatures, the training dataset is divided into several several sub-datasets, resulting from a k-mean clustering. This ensure that, in each sub-dataset, a linear relationship is a good approximation between the observations and the temperature and different linear regression coefficient are computed for each sub-dataset.~~

We compared the ANN retrievals with this reprocessed EUMETSAT CDR~~dataset~~. Since the two methods use the same IASI observations input, there is no need for an interpolation over the coordinates of the observations. However, EUMETSAT temperatures profiles are retrieved on 138 levels, reflecting the 137 hybrid levels from the ERA-5 L137 grid plus the surface level, so we interpolated EUMETSAT temperatures to the fixed pressure levels of the ANN. Figure ~~7~~9 shows the differences between the zonal mean temperatures of the ANN output and EUMETSAT.

The differences are small at all pressure levels (less than 0.5 K) except at 2 hPa where they can reach 1 K, and we see seasonal variations of the differences that are more pronounced in the troposphere (750, 550 and 400 hPa). At 7, 10 and 70

hPa, the differences are positive and larger at the equator and they decrease over time. This bias can also be seen at higher latitudes and other pressure levels, although it is less obvious. This bias might be due to the fact that EUMETSAT's algorithm does not use CO_2 in input and the retrieval is impacted by the variations of the CO_2 over time, which we account for.

Note that although the ANN and EUMETSAT retrievals are both based on IASI radiances, the two temperature records are not redundant: EUMETSAT will keep on doing minor updates but not reprocessed the data back in time, whereas our dataset can constantly be enhanced and updated rapidly. Moreover the two datasets use different observations (IASI radiances and CO_2 concentrations for the ANN, and IASI, AMSU and MHS radiances for EUMETSAT) and different methods of retrieval (ANN and PWLR[3]). Note that although the ANN and EUMETSAT retrievals are both based on IASI radiances, the two temperature records are not redundant. The two datasets use different observations (IASI radiances and CO_2 concentrations for the ANN, and IASI, AMSU and MHS radiances for EUMETSAT) and different methods of retrieval (ANN and PWLR[3]). When needed, our dataset can constantly be enhanced and rapidly reprocessed for the entire time series. EUMETSAT CDR can be produced for every major change in the operational real time all-sky temperature processor.

54 Applications

We used the ANN temperatures to compute trends over the past 13 years. One of IASI's main assets is its high radiometric stability over the years and it is used as a reference for the inter-calibration of infrared sensors by the Global Space-Based Inter-Calibration System (Golberg et al., 2011) so temperatures derived from IASI radiances are a good product to study atmospheric trends.

We use IASI daily zonal mean temperature (latitude bands of 1°) and we compute the Theil-Sen estimator for each latitude and each pressure level. The Theil-Sen estimator is a robust method for computing linear trends, where the trends is determined by the median of all the possible slopes between pairs of points (Theil, 1950; Sen, 1968). We also computed the associated p-values, with a 0.05 threshold for significance being considered. Before the Theil-Sen estimator was applied, we removed the contributions of El Niño-Southern Oscillation (ENSO) and the QBO to temperatures. Their contribution was computed using a multiple linear regression based on the Multivariate ENSO Index (MEI, https://psl.noaa.gov/enso/mei/) and the QBO30 and QBO50 indices (equatorial zonal winds at 30 and 50 hPa, https://www.cpc.ncep.noaa.gov/data/indices/). Figure 810 shows the significant temperature trends for the 2008-2020 period. Non-significant trends are shown in grey in Figure 810.

We clearly see a warming in the troposphere. In the tropics, we see a warming of 0.2-0.3 K/decadeAt the equator,

~~temperature increases by 0.7 K/decade in the upper troposphere, and 0.5 K/decade in the lower troposphere.~~ At mid latitude, the warming is ~~weaker~~stronger (0.5-0.6 K/decade). As highlighted by previous studies (Masson-Delmotte et al., 2021~~IPCC, 2014~~), the poles are where tropospheric temperatures are warming the quickest, especially the Arctic, where temperatures increase by 1 K/decade (arctic amplification). The values of the trends we found between 45°S and 45°N are similar to those

415   found by Shangguan et al. (2019)~~, although the areas of strongest warming are slightly different~~.

In the stratosphere, we observe a cooling at all latitudes north of 40°S ~~almost everywhere except from 40°S northwards~~. The cooling is strongest at the equator, above 20 hPa (-1 K/decade). In the Arctic, there is no significant trend. This cooling of the stratosphere has also been observed by Maycock et al. (2018) and Randel et al. (2016), although their values are ~~inferior~~

420   smaller than~~to~~ those found here (but their time period is also different). In the Southern Hemisphere, we see two areas of warming: a strong one at 50°S and 100 hPa (1 K/decade) and another located at 80°S and 10 hPa (0.4 K/decade). Part of this warming is due to a sudden stratospheric warming (SSW) that happened in September 2019 (Safieddine et al., 2020b). The temperature increased by more than 30 K in a few days. Such a warming toward the end of our study period has a strong impact on trends. However, the computation of trends over the period 2008-2018 still shows warming in these two regions

425   and it cannot all be attributed to the SSW. The warming is weaker at 50°S-100 hPa (0.6 K/decade) and stronger at 80°S-10 hPa (0.8 K/decade). Due to the Montreal Protocole in 1987, the ozone hole has been recovering since the 1990's (WMO, 2018; Weber et al., 2018; Strahan et al., 2019), and warming in the stratospheric south pole can partly be attributed to this recovery.

430   Figure 11 shows the temperature time series in the regions delimited by dashed rectangles in Figure 10. The time series are shown with and without the contributions of ENSO and QBO. In the equatorial troposphere, we see that temperature are increasing. However, removing the contribution of ENSO significantly reduces the warming trend, as most of it was driven by the strong El Niño event of 2015-2016. In the Arctic troposphere, there is no significant differences in the time series with and without the contribution of ENSO/QBO, suggesting that these phenomena does not have a large impact on Arctic

435   temperature, and the warming observed in this region is due to the increase of greenhouse gases and Arctic amplification. In the Southern stratosphere, the trend in both warming regions seem to be driven by the 2019 SSW. However, we see a continuous increase of temperatures before 2019 (with and without ENSO/QBO contribution) that cannot be attributed to the SSW and is most likely due to ozone hole recovery.

440

We also computed trends with ERA5 and ARSA (supplementary material, Figure S3~~2~~ and S3~~4~~). ERA5 trends are very similar to those of IASI retrievals, except for a strong warming over the Arctic between 2 and 7 hPa (1 K/decade). With ARSA, we see a warming between 0.5 and 1 K/decade in Antarctica at all altitudes except 2 hPa. In Greenland, we also see a warming at almost all altitudes, but weaker (between 0 and 0.5 K/decade). In all the other regions, we see a warming

445 between 750 and 200 or 100 hPa and a cooling above 100 hPa. The tropospheric warming and stratospheric cooling are more important in the Pacific than in the other regions. In the Arabian Peninsula, we see a smaller warming below 200 hPa than in the other regions. These results are coherent with the trends computed with IASI and ERA5.

5 Conclusion

We use an artificial neural network to construct a homogeneous temperature record from IASI radiances. ~~This dataset is~~
450 ~~available from https://iasi ft.eu/products/atmospheric temperature profiles/ (doi for Metop A temperatures:10.21413/IASI FT_METOPA_ATP_L3_LATMOS ULB and doi for Metop B temperatures: 10.21413/IASI FT_METOPB_ATP_L3_LATMOS ULB)~~. Validation of the IASI ANN product with ERA5, ARSA and EUMETSAT reprocessed temperatures shows a good agreement between the four datasets especially between 7 and 750 hPa. The differences between IASI ANN temperatures and ERA5 are less than ~~inferior to~~ 0.5 K at most latitudes and most
455 pressure levels, and the differences between IASI and ARSA are similar, demonstrating~~, if needed,~~ that our IASI product can be used to assess local variation of temperature and to compute trends.

We used these temperatures to compute trends over the 2008-2020 period. We found a warming trend in~~an increase of~~ tropospheric temperatures, stronger at mid latitudes ~~in the equatorial upper troposphere~~ (0.5~~75~~ K/decade) and at the poles (1
460 K/decade due to arctic amplification). ~~. We also see a strong stratospheric cooling between 30°S and 30°N. In the Southern stratosphere (40°S to 90°S), there are two regions with important warming due to the ozone hole recovery.~~ In the stratosphere, we found a strong cooling trend in the tropics between 30°S and 30°N while poleward of 40°S there are two regions with important warming due to the ozone hole recovery and a SSW that happened in 2019.

465 This work shows that artificial neural networks are efficient to retrieve atmospheric temperatures from huge datasets of radiance. With this method, temperature profiles from all 10 billion observations from Metop-A and B can be computed in two days. With the short computation time and with IASI radiances being available a few hours after the observations, we can obtain temperature profiles in near real time.

470 We now have a homogeneous product to study seasonal and climatological variations of temperatures. It can also be used to study extreme events such as El Niño-Southern Oscillation, volcanic eruptions, heatwaves, sudden stratospheric warmings, and their link with climate change.

Although the trends computed with the ANN retrievals are coherent with other studies, a 13-year period is slightly too short
475 for them to be fully reliable, and they can be impacted by short-term variation of temperatures (El-Niño Southern Oscillation for example). Chédin et al. (2016) showed that the number of years required to meet the probability assigned criterion with

the Theil-Sen estimator is 14-15 years. However, these results are promising: since IASI is planned to fly for at least another few years, the trends will become more and more reliable as the record gets longer. From 2024 onwards the IASI-NG missions onboard Metop-SG (Crevoisier et al, 2014) will continue the IASI record, allowing to derive trends on longer timescales.

Data availability

EUMETSAT reprocessed L1C and L2 data are available at https://doi.org/10.15770/EUM_SEC_CLM_0014 https://doi.org/10.15770/EUM_SEC_CLM_0027, respectively. ERA5 data can be downloaded from the Copernicus Climate Change Service Climate Data Store : https://cds.climate.copernicus.eu/cdsapp#!/dataset/reanalysis-era5-pressure-levels?tab=overview. Requests for ARSA temperatures can be made at: https://ara.lmd.polytechnique.fr/index.php?page=arsa. The temperatures retrieved with the ANN can be downloaded at https://iasi-ft.eu/products/atmospheric-temperature-profiles/ (doi for Metop-A temperatures: https://doi.org/hbxm and doi for Metop-B temperatures: https://doi.org/hbxn).

Author contributions

M.B. designed the ANN to retrieve the temperatures, performed the validation and prepared the manuscript with contributions from all co-authors. S.W and L.C. provided the reader for L1C data. F.A and V.P provided the selection S1 and O.L provided the selection S2. N.S. provided ARSA temperatures and helpful explanations on their construction. M.DB. provided informations on EUMETSAT L2 dataCDR. This work was supervised by S.S. and C.C.

Competing interests

The authors declare that they have no conflict of interest.

Acknowledgments

We would like to thank the reviewers for their thoughtful comments and efforts towards improving our manuscript. IASI has been developed and built under the responsibility of the Centre National d'Etudes spatiales (CNES, France). It is on board the Metop satellites as part of the EUMETSAT Polar System. The IASI L1C data are received through the EUMETCast near-real-time data distribution service. This project has received funding from the European Research Council (ERC) under the European Union's Horizon 2020 research and innovation program (grant agreement No 742909). It was also supported by the Prodex arrangement IASI.FLOW (Belspo-ESA). L. Clarisse is a research associate (Chercheur Qualifié) supported by the

Belgian F.R.S.-FNRS. The LATMOS team is grateful to CNES for scientific collaboration and financial support. We thank
505 EUMETSAT for providing us a full reprocessed dataset of radiances with the latest version of the L1C. We also thank
Juliette Hadji-Lazaro and Philippe Keckhut for their help.

References

Aires, F., Chédin, A., Scott, N. A. and Rossow, W/ B.: A regularized neural net approach for retrieval of atmospheric and
surface temperatures with the IASI instrument, J. Appl. Meteorol., 41, 144-159, doi: 10.1175/1520-
510 0450(2002)041%3C0144:ARNNAF%3E2.0.CO;2, 2002.

Aquila, V., Swartz, W. H., Waugh, D. W., Colarco, P. R., Pawson, S., Polvani, L. M. and Stolarski, R. S.: Isolating the roles
of different forcing agents in global stratospheric temperature changes using model integrations with incrementally added
single forcings, J. Geophys. Res.-Atmos., 121 (13), 8067-8082, doi:10.1002/2015JD023841, 2016.

515

Bormann, N., Bonavita, M., Dragani, R., Eresmaa, R., Matricardi, M. and , McNally, A.: Enhancing the impact of IASI
observations through an updated observation-error covariance matrix, Q. J. Roy. Meteor. Soc., 142, 1767–1780,
doi:10.1002/qj.2774, 2016.

520 Bouillon, M., Safieddine, S., Hadji-Lazaro, J., Whitburn, S., Clarisse, L., Doutriaux-Boucher, M., Coppens, D., August, T.,
Jacquette, E,, Clerbaux, C.: Ten-year assessment of IASI radiance and temperature, Remote Sens., *12*, 2393,
doi:10.3390/rs12152393, 2020.

Boynard, A., Hurtmans, D., Garane, K., Goutail, F., Hadji-Lazaro, J., Koukouli, M. E., Wespes, C., Vigouroux, C., Keppens,
525 A., Pommereau, J.-P., Pazmino, A., Balis, D., Loyola, D., Valks, P., Sussmann, R., Smale, D., Coheur, P.-F., and Clerbaux,
C.: Validation of the IASI FORLI/EUMETSAT ozone products using satellite (GOME-2), ground-based (Brewer–Dobson,
SAOZ, FTIR) and ozonesonde measurements, Atmos. Meas. Tech., 11, 5125–5152, doi:10.5194/amt-11-5125-2018, 2018.

Chédin, A., Serrar, S., Scott, N. A., Crévoisier, C., and Armante R.: First global measurement of midtropospheric CO2 from
530 NOAA polar satellites: Tropical zone, J. Geophys. Res., 108, 4581, doi:10.1029/2003JD003439, 2003.

Chédin, A., Capelle, V., and Scott, N.A.: Detection of IASI dust AOD trends over Sahara: How many years of data required
?, Atmos. Res., 212,120-129, doi: 10.1016/j.atmosres.2018.05.004, 2018.

535 Clarisse, L., R'Honi, Y., Coheur, P.-F., Hurtmans, D., and Clerbaux, C.: Thermal infrared nadir observations of 24 atmospheric gases, Geophys. Res. Lett., 38, doi:10.1029/2011GL047271, 2011.

Clerbaux, C., Boynard, A., Clarisse, L., George, M., Hadji-Lazaro, J., Herbin, H., Hurtmans, D., Pommier, M., Razavi, A., Turquety, S., Wespes, C., and Coheur, P.-F.: Monitoring of atmospheric composition using the thermal infrared IASI/MetOp

540 sounder, Atmos. Chem. Phys., 9, 6041–6054, doi:10.5194/acp-9-6041-2009, 2009.

Collard, A.: Selection of IASI channels for use in numerical weather prediction, Q. J. Roy. Meteor. Soc., 133, 1977–1991, doi:10.1002/qj.178, 2007.

545 Copernicus Climate Change Service (C3S): ERA5: Fifth generation of ECMWF atmospheric reanalyses of the global climate. Copernicus Climate Change Service Data Store (CDS), available online: https://cds.climate.copernicus.eu/cdsapp#!/home/ (accessed on 31 August 2019).

Crevoisier, C., Clerbaux, C., Guidard, V., Phulpin, T., Armante, R., Barret, B., Camy-Peyret, C., Chaboureau, J.-P., Coheur,

550 P.-F., Crépeau, L., Dufour, G., Labonnote, L., Lavanant, L., Hadji-Lazaro, J., Herbin, H., Jacquinet-Husson, N., Payan, S., Péquignot, E., Pierangelo, C., Sellitto, P., and Stubenrauch, C.: Towards IASI-New Generation (IASI-NG): impact of improved spectral resolution and radiometric noise on the retrieval of thermodynamic, chemistry and climate variables, Atmos. Meas. Tech., 7, 4367–4385, doi:10.5194/amt-7-4367-2014, 2014.

555 Dee, D. P., Uppala, S. M., Simmons, A. J., Berrisford, P., Poli, P., Kobayashi, S., Andrae, U., Balmaseda, M. A., Balsamo G., Bauer, P., Bechtold, P., Beljaars, A. C. M., van de Berg, L., Bidlot, J., Bormann, N., Delsol, C., Dragani, R., Fuentes, M., Geer, A. J., Haimberger, L., Healy, S. B., Hersbach, H., Hólm, E. V., Isaksen, L., Kållberg, P., Köhler, M., Matricardi, M., McNally, A. P., Monge-Sanz, B. M., Morcrette, J. J., Park, B. K., Peubey, C, de Rosnay, P., Tavolato, C., Thépaut, J. N., and Vitart, F.: The ERA-Interim reanalysis: configuration and performance of the data

560 assimilation system, Q. J. Roy. Meteor. Soc., (137-656), 553-597, doi: 10.1002/qj.828, 2011.

ECMWF: IFS documentation-CY43R1. Part IV: physical processes », Reading, UK, 2016.

EUMETSAT: IASI L2 Metop-B–validation report, EUMETSAT, Darmstadt, Germany,

565 https://www.eumetsat.int/media/45985, 2013a, 2013a.

EUMETSAT: HIRS Level 1 product format specification, https://www.eumetsat.int/media/38677, 2013b.

EUMETSAT: EUMETSAT annual report 2017, https://www.eumetsat.int/media/42734, 2017.

570

EUMETSAT: Validation report IASI Level2 T and Q profiles release 1,https://www.eumetsat.int/media/47744, doi: 10.15770/EUM_SEC_CLM_0027, 2020.

George, M., Clerbaux, C., Bouarar, I., Coheur, P.-F., Deeter, M. N., Edwards, D. P., Francis, G., Gille, J. C., Hadji-Lazaro, J., Hurtmans, D., Inness, A., Mao, D., and Worden, H. M.: An examination of the long-term CO records from MOPITT and IASI: comparison of retrieval methodology, Atmos. Meas. Tech., 8, 4313–4328, doi:10.5194/amt-8-4313-2015, 2015.

Goldberg, M., Ohring, G., Butler, J., Cao, C., Datla, R., Doelling, D., Gärtner, V., Hewison, T., Iacovazzi, B., Kim, D., Kurino, T., Lafeuille, J., Minnis, P., Renaut, D., Schmetz, J., Tobin, D., Wang, L., Weng, F., Wu, X., Yu, F., Zhang, P., and Zhu, T.: The Global Space-Based Inter-Calibration System, Bull. Amer. Meteor. Soc., 92, 467-475, doi: 10.1175/2010BAMS2967.1, 2011.

Hans, I., Burgdorf, M., Buehler, S. A., Prange, M., Lang, T., and John, V.O.: MHS microwave humidity sounder climate data record release 1 - Metop and NOAA, European Organisation for the Exploitation of Meteorological Satellites, doi: 10.15770/EUM_SEC_CLM_0045, 2020.

Hersbach, H., de Rosnay, P., Bell, B., Schepers, D., Simmons, A., Soci, C., Abdalla, S., Alonso-Balmaseda, M., Balsamo, G., Bechtold, P., Berrisford, P., Bidlot, J.-R., de Boisséson, E., Bonavita, M., Browne, P., Buizza, R., Dahlgren, P., Dee, D., Dragani, R., Diamantakis, M., Flemming, J., Forbes, R., Geer, A. J., Haiden, T., Hólm, E., Haimberger, L., Hogan, R., Horányi, A., Janiskova, M., Laloyaux, P., Lopez, P., Munoz-Sabater, J., Peubey, C., Radu, R., Richardson, D., Thépaut, J.-N., Vitart, F., Yang, X., Zsótér, E. and Zuo, H.: Operational global reanalysis: progress, future directions and synergies with NWP, Era5 Report Series, available online: https://www.ecmwf.int/en/elibrary/18765-operational-global-reanalysis-progress-future-directions-and-synergies-nwp (accessed on 31 August 2019).

Hilton, F., Armante, R., August, T., Barnet, C., Bouchard, A., Camy-Peyret, C., Capelle, V., Clarisse, L., Clerbaux, C, Coheur, P.-F., Collard, A., Crevoisier, C., Dufour, G., Edwards, D., Faijan, F., Fourrié, N., Gambacorta, A., Goldberg, M., Guidard, V., Hurtmans, D., Illingworth, S., Jacquinet-Husson, N., Kerzenmacher, T., Klaes, D., Lavanant, L., Masiello, G., Matricardi, M., McNally, A., Newman, S., Pavelin, E., Payan, S., Péquignot, E., Peyridieu, S., Phulpin, T., Remedios, J., Schlüssel, P., Serio, C., Strow, L., Stubenrauch, C., Taylor, J., Tobin, D., Wolf, W., and Zhou, D.: Hyperspectral Earth observation from IASI: five years of accomplishments, Bull. Amer. Meteor. Soc., 93, 347-370, doi:10.1175/BAMS-D-11-00027.1, 2012.

~~IPCC: Intergovernmental panel on climate change fifth assessment report, Geneva, Switzerland, 2014.~~

605 Lambrigtsen, B. H., Fetzer, E., Fishbein, E., Lee, S.-Y., and Pagano, T.: AIRS - the atmospheric infrared sounder, IEEE International Geoscience and Remote Sensing Symposium, doi:10.1109/IGARSS.2004.1370798, 2004.

Li, J., Wang, M.-H., and Ho, Y.-S.: Trends in research on global climate change: a science citation index expanded-based analysis. Glob. Planet. Chang., 77, 13–20, doi:10.1016/j.gloplacha.2011.02.005, 2011.

610

Masson-Delmotte, V., Zhai, P., Pirani, A., Connors, S.L., Péan, C., Berger, S., Caud, N., Chen, Y., Goldfarb, L., Gomis, M.I., Huang, M., Leitzell, K., Lonnoy, E., Matthews, J.B.R, Maycock, T,K., Waterfield, T., Yelekçi, O., Yu, R., and Zhou, B.: IPCC, 2021: Climate Change 2021: The Physical Science Basis. Contribution of Working Group I to the Sixth Assessment Report of the Intergovernmental Panel on Climate Change, Cambridge University Press. In Press., 2021.

615

Maycock, A. C., Randel, W. J., Steiner, A. K., Karpechko, A. Y., Christy, J., Saunders, R., Thompson, D. W. J., Zou, C.-Z., Chrysanthou, A., Luke Abraham, N., Akiyoshi, H., Archibald, A. T., Butchart, N., Chipperfield, M., Dameris, M., Deushi, M., Dhomse, S., Di Genova, G., Jöckel, P., Kinnison, D. E., Kirner, O., Ladstädter, F., Michou, M., Morgenstern, O., O'Connor, F., Oman, L., Pitari, G., Plummer, D. A., Revell, L. E., Rozanov, E., Stenke, A., Visioni, D., Yamashita, Y., and 620 Zeng, G.: Revisiting the mystery of recent stratospheric temperature trends, Geophys. Res. Lett., 45, 9919– 9933, doi:10.1029/2018GL078035, 2018.

McLaren, A., Fiedler, E., Roberts-Jones, J., Martin, M., Mao, C., and Good, S.: Quality information document global ocean OSTIA near real time level 4 sea surface temperature product SSTGLO-SST-L4-NRT-OBSERVATIONS-010-001, EU 625 Copernicus Marine Service. 2016. Available online: https: //resources.marine.copernicus.eu/documents/QUID/CMEMS-OSI-QUID-010-001.pdf (accessed on 24 July 2020).

Moncet, J.-L., Uymin, G., Liang, P. and Lipton, A.E.: Fast and accurate radiative transfer in the thermal regime by 630 simultaneous optimal spectral sampling over all channels, J. Atmos. Sci., 72, 2622–2641, doi: 10.1175/JAS-D-14-0190.1, 2015.

Parracho, A. C., Safieddine, S., Lezeaux, O., Clarisse, L., Whitburn, S., George, M., Prunet, P., and Clerbaux, C.: IASI-derived sea surface temperature data set for climate, Earth Space Sci., 8, e2020EA001427 . doi:10.1029/2020EA001427, 635 2021.

Pellet, V. and Aires, F.: Bottleneck channels algorithm for satellite data dimension reduction: a case study for IASI, IEEE Trans. Geosci. Remote Sens, 56 (10), 6069-6081, doi: 10.1109/TGRS.2018.2830123, 2018.

640 Rabier, F., Fourrié, N., Chafäi, D. and P. Prunet: Channel selection methods for Infrared Atmospheric Sounding Interferometer radiances, Q. J. Roy. Meteor. Soc., 128(581), 1011–1027, doi: 10.1256/0035900021643638, 2002.

Randel, W. J., Smith, A. K., Wu, F., Zou, C.-Z., and Qian, H.: Stratospheric temperature trends over 1979–2015 derived from combined SSU, MLS, and SABER satellite observations, J. Climate, 29, 4843–4859, doi:10.1175/JCLI-D-15-0629.1, 645 2016.

Reale, A., Tilley, F., Ferguson, M., and Allegrino, A.: NOAA operational sounding products for advanced TOVS, Int. J. Remote Sens., 29, 4615-4651, doi: 10.1080/01431160802020502, 2008.

650 Rodgers, C. D.: Inverse Methods for Atmospheric Sounding: Theory and Practice, World Scientific Publishing, London, UK, 2000.

Safieddine, S., Parracho, A. C., George, M., Aires, F., Pellet, V., Clarisse, L., Whitburn, S., Lezeaux, O., Thépaut, J.-N., Hersbach, H., Radnoti, G., Goettsche, F., Martin, M., Doutriaux-Boucher, M., Coppens, D., August, T., Zhou, D.K., and 655 Clerbaux, C.: Artificial neural network to retrieve land and sea skin temperature from IASI, Remote Sens., 12, 2777, doi: 10.3390/rs12172777, 2020a.

Safieddine, S., Bouillon, M., Parracho, A. C., Jumelet, J., Tencé, F., Pazmino, A., Goutail, F., Wespes, C., Bekki, S., 665 Boynard, A., Hadji-Lazaro, J., Coheur, P.F., Hurtmans, D., and Clerbaux, C.: Antarctic ozone enhancement during the 2019 sudden stratospheric warming event, Geophys. Res. Lett., 47, e2020GL087810, doi:10.1029/2020GL087810, 2020b.

Santer, B. D., Solomon, S., Wentz, F .J., Fu, Q., Po-Chedley, S., Mears, C., Painter, J. F., and Bonfils, C.: Tropospheric warming over the past two decades, Sci. Rep., 7, 2336, doi:10.1038/s41598-017-02520-7, 2017.
670
Saunders, R., Hocking, J., Turner, E., Rayer, P., Rundle, D., Brunel, P., Vidot, J., Roquet, P., Matricardi, M., Geer, A., Bormann, N. and Lupu, C.: An update on the RTTOV fast radiative transfer model (currently at version 12), Geosci. Model Dev., 11, 2717-2737, doi: 10.5194/gmd-11-2717-2018, 2018.

675   Scott, N. A. and Chédin, A.: A fast line-by-line method for atmospheric absorption computations: the automatized atmospheric absorption atlas, J. Appl. Meteor., 20(7), 802-812, doi: 10.1175/1520-0450(1981)020%3C0802:AFLBLM%3E2.0.CO;2, 1981.

Scott, N. A., Chédin, A., Pernin, J., Armante, R., Capelle, V., and Crépeau, L.: QUASAR: quality assessment of satellite and
680   radiosonde data, 2015.

Seidel, D. J., Berger, F. H., Immler, F., Sommer, M., Vömel, H., Diamond, H. J., Dykema, J., Goodrich, D., Murray, W., Peterson, T., Sisterson, D., Thorne, P., and Wang, J.: Reference upper-air observations for climate: rationale, progress, and plans, B. Am. Meteorol. Soc., 90, 361–369, doi:10.1175/2008BAMS2540.1, 2009.

685

Sen, P. K.: Estimates of the regression coefficient based on Kendall's tau, J. Am. Stat. Assoc., 63(324), 1379-1389, doi: 10.1080/01621459.1968.10480934, 1968.

Shangguan, M., Wang, W., and Jin, S.: Variability of temperature and ozone in the upper troposphere and lower stratosphere
690   from multi-satellite observations and reanalysis data, Atmos. Chem. Phys., 19, 6659–6679, doi:10.5194/acp-19-6659-2019, 2019.

Susskind, J., Schmidt, G. A., Lee, J. N., and Iredell, L.: Recent global warming as confirmed by AIRS, Environ. Res. Lett., 14, 044030. doi:10.1088/1748-9326/aafd4e, 2019.

695

Tett, S. F. B., Jones, G. S., Stott, P. A., Hill, D. C., Mitchell, J. F. B., Allen, M. R., Ingram, W. J., Johns, T. C., Johnson, C. E., Jones, A., Roberts, D. L., Sexton, D. M. H., and Woodage, M. J.: Estimation of natural and anthropogenic contributions to twentieth century temperature change, J. Geophys. Res., 107, 4306, doi:10.1029/2000JD000028, 2002.

700   Theil, H.: A rank-invariant method of linear and polynomial regression analysis. I, II, III", Nederl. Akad. Wetensch., Proc., 53, 386–392, 521–525, 1397–1412, 1950.

Van Damme, M., Whitburn, S., Clarisse, L., Clerbaux, C., Hurtmans, D., and Coheur, P.-F.: Version 2 of the IASI NH_3 neural network retrieval algorithm: near-real-time and reanalysed datasets, Atmos. Meas. Tech., 10, 4905–4914,
705   doi:10.5194/amt-10-4905-2017, 2017.

Yang, J., Gong, P., Fu, R., Zhang., M., Chen, J., Liang, S., Xu, B., Shi, J., and Dickinson, R.: The role of satellite remote sensing in climate change studies. Nature Clim Change, 3, 875–883, doi:10.1038/nclimate1908, 2013.

710   Zou, C.-Z., Qian, H., Wang, W., Wang, L., and Long, C.: Recalibration and merging of SSU observations for stratospheric temperature trend studies, J. Geophys. Res.-Atmos., 119, 13,180-13,205, doi:10.1002/2014JD021603, 2014.

715
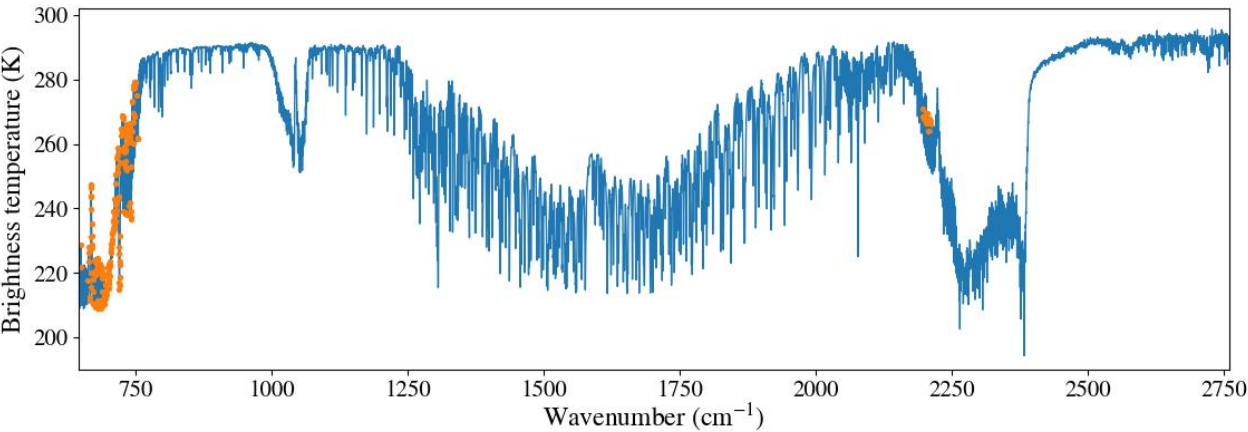
Figure 1: IASI clear-sky spectrum in brightness temperature in K (blue), with the selected channels in orange

720
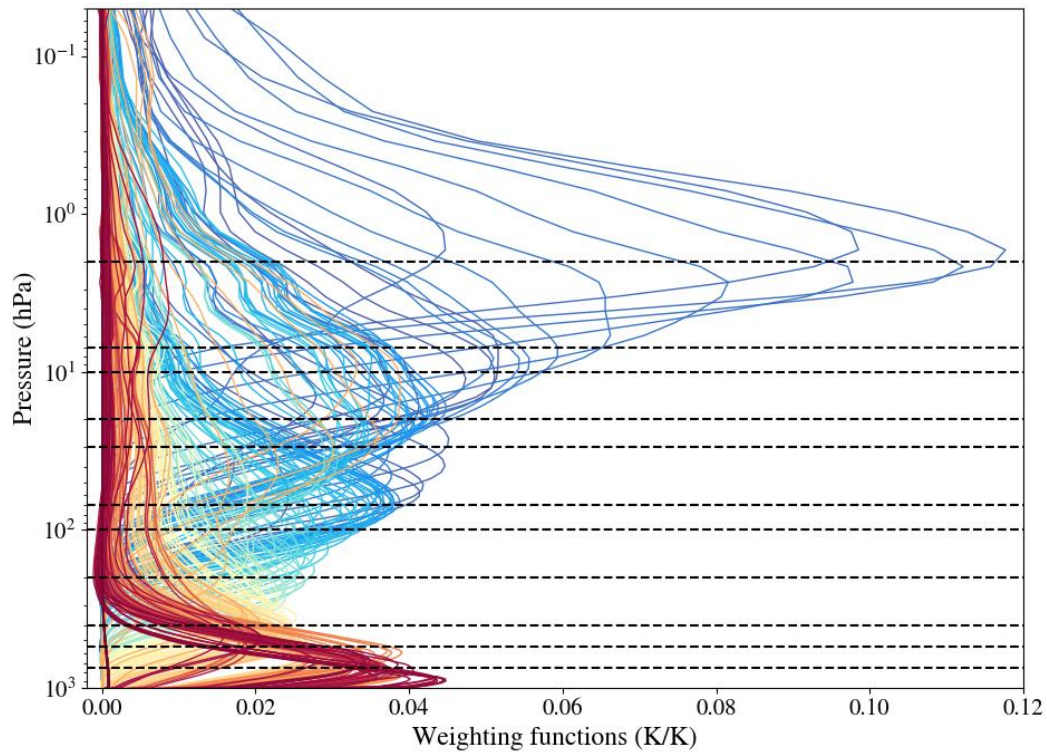
Figure 2: ~~Jacobians~~ Weighting functions for the 231 selected IASI channels. Horizontal dashed lines represent the 11 pressure levels for which the temperatures are computed. The colors of the ~~jacobians~~ weighting functions represent the wavenumbers of the selected channels (blue for the channels around 700 cm⁻¹, red for the channels around 2200 cm⁻¹).

730
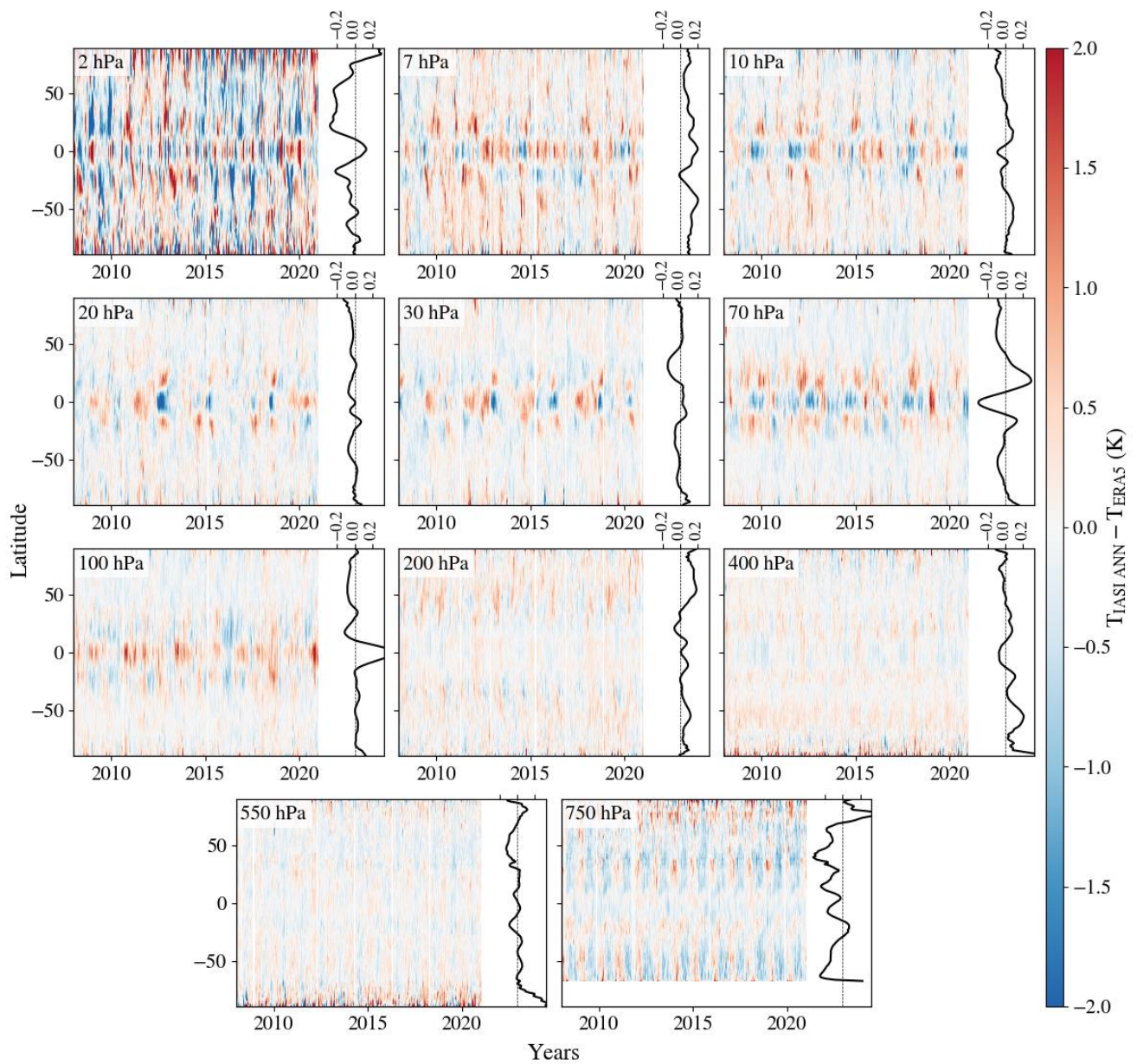
Figure 3: Daily zonal mean differences between IASI and ERA5 zonal mean temperature for the 11 pressure levels of the ANN, with the time averaged differences on the right of each subplot.
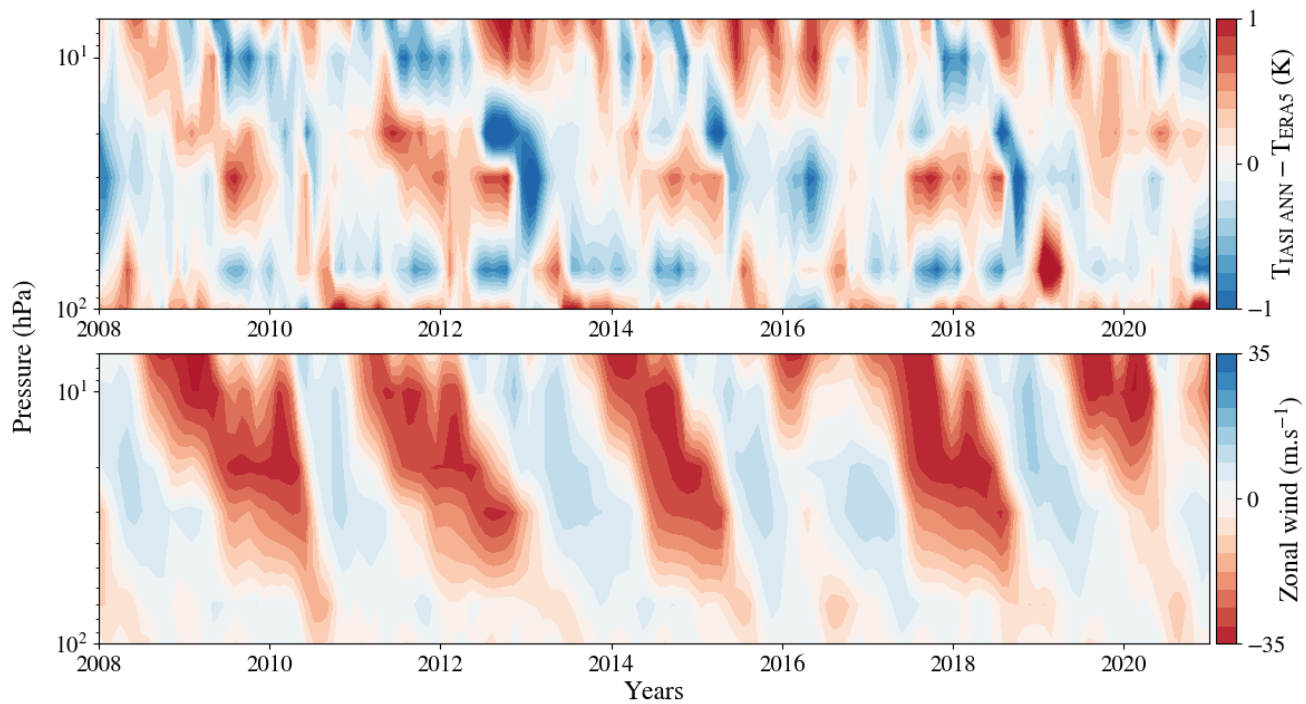
Figure 4: Monthly mean of the temperature differences between IASI-ANN and ERA5 (top) and monthly zonal wind from ERA5 (bottom) between 10°S and 10°N.

740
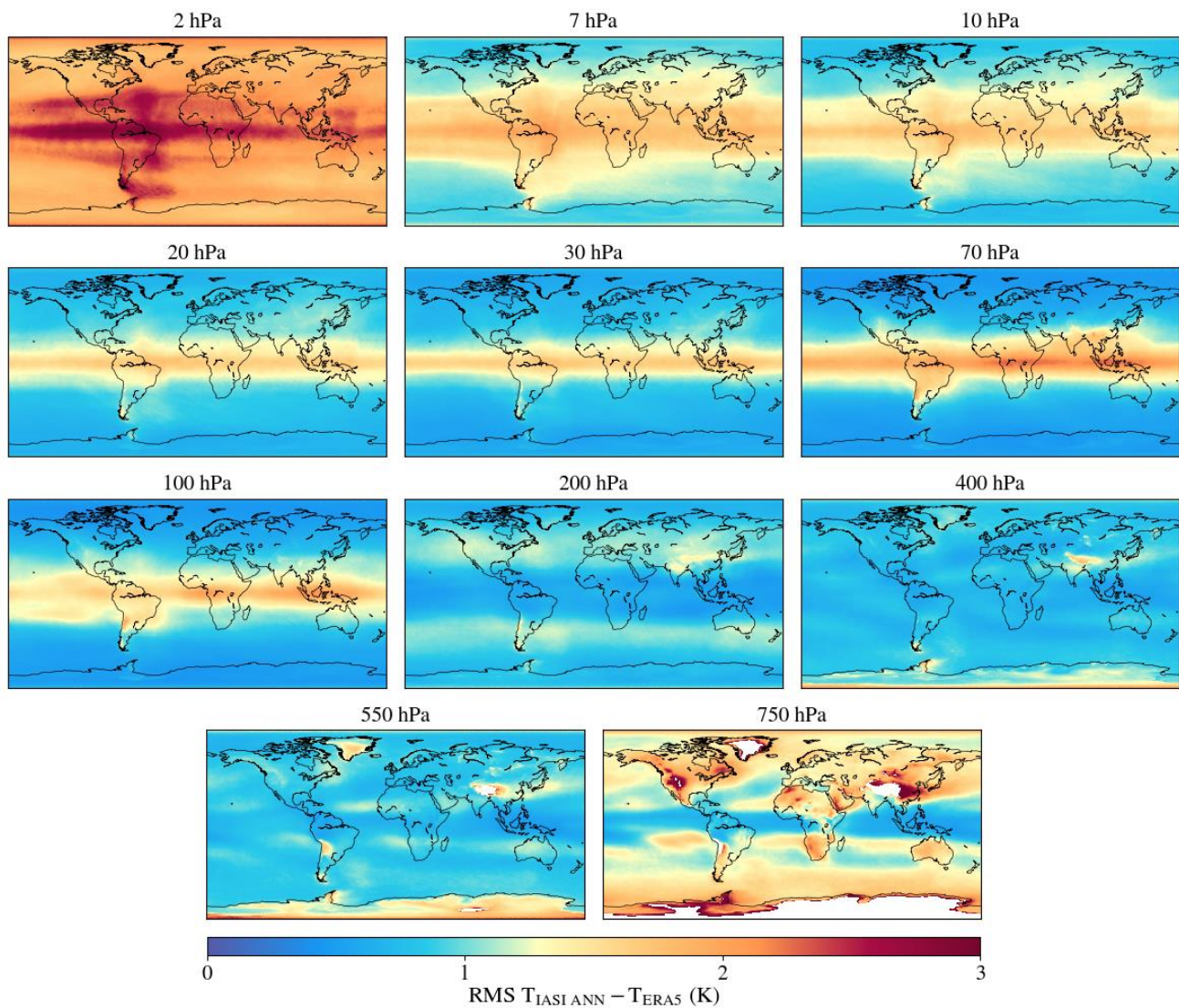
745 **Figure 54: RMS of the daily differences between IASI retrievals and ERA5 in 1°×1° latitude-longitude grid over the period 2008-2020.**
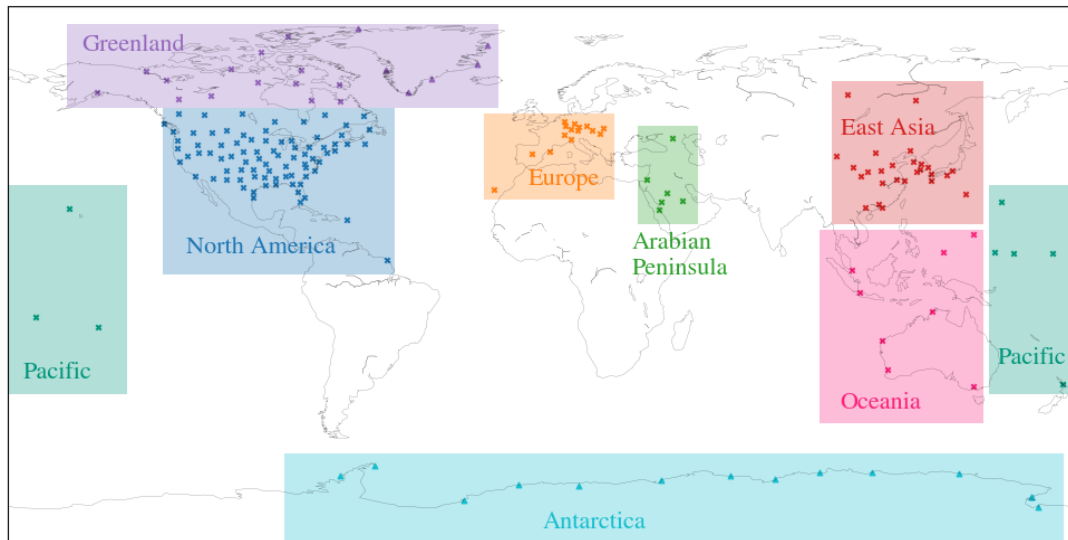
Figure 65: Locations of the ARSA stations with at least 300 observations per year (crosses) and the stations in two other regions (Greenland and Antarctica) that do not satisfy this condition are marked in triangles. The rectangles of color correspond to the regions in which we compared IASI temperatures to ARSA.
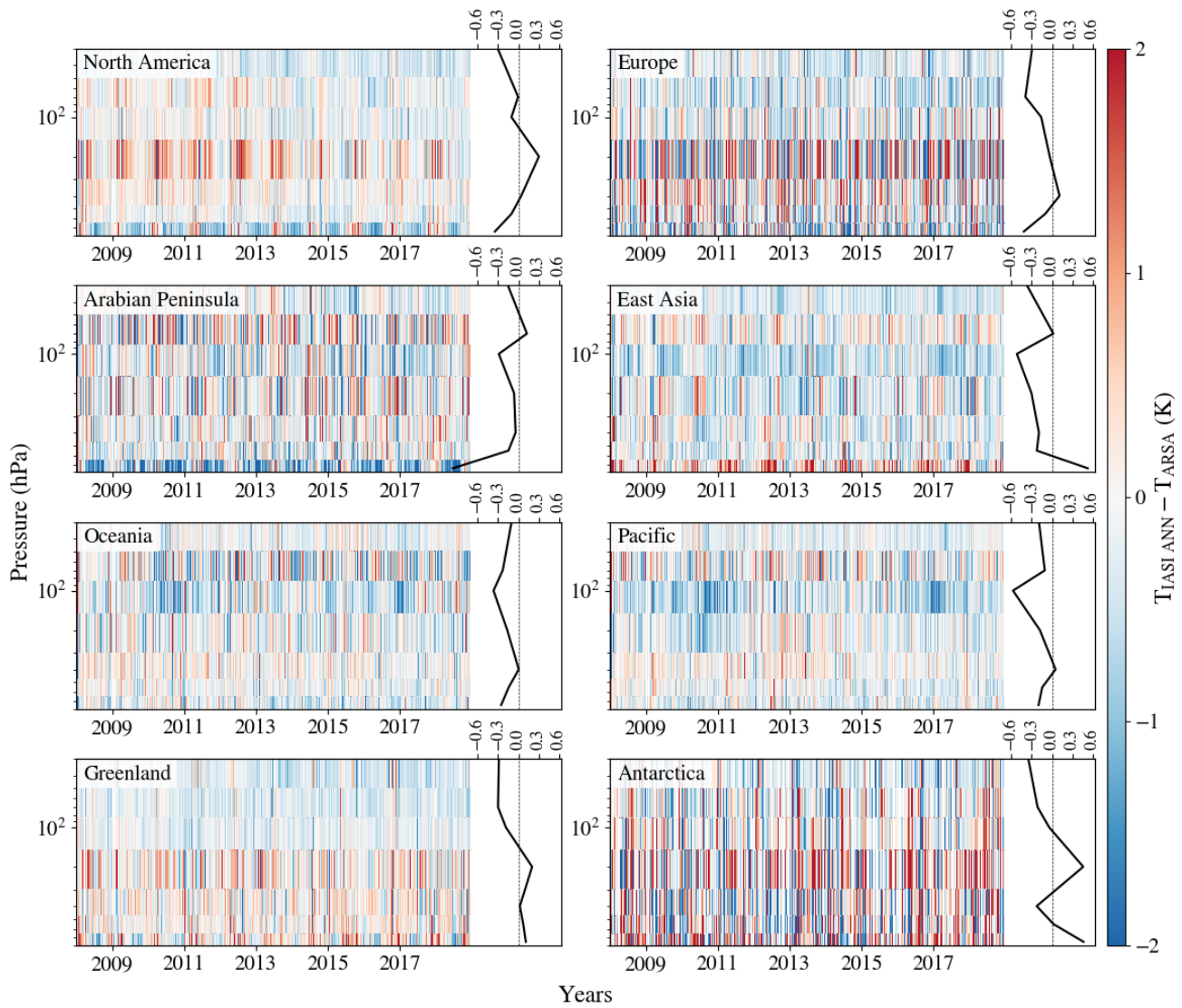
Figure 76: Dayly differences between IASI-ANN and ARSA temperatures between 2008 and 2018 in North America, Europe, the Arabian Peninsula, East Asia, Oceania, the Pacific, Greenland and Antarctica, with the time average differences profiles on the right of each subplot.
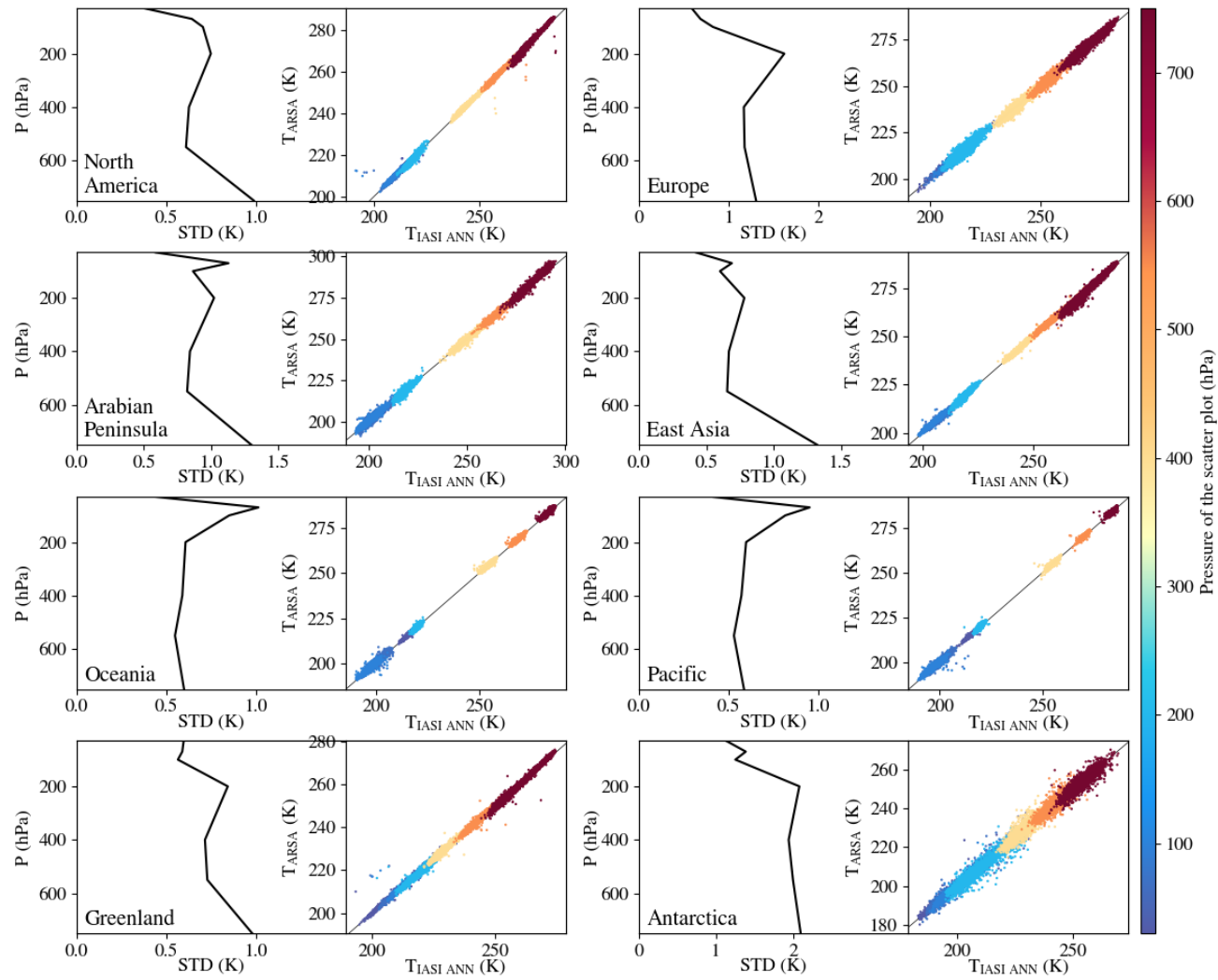
Figure 8: Standard deviation profiles of the differences between IASI-ANN and ARSA temperatures (left of each subplot) and correlation between the two dataset (right of each subplot).
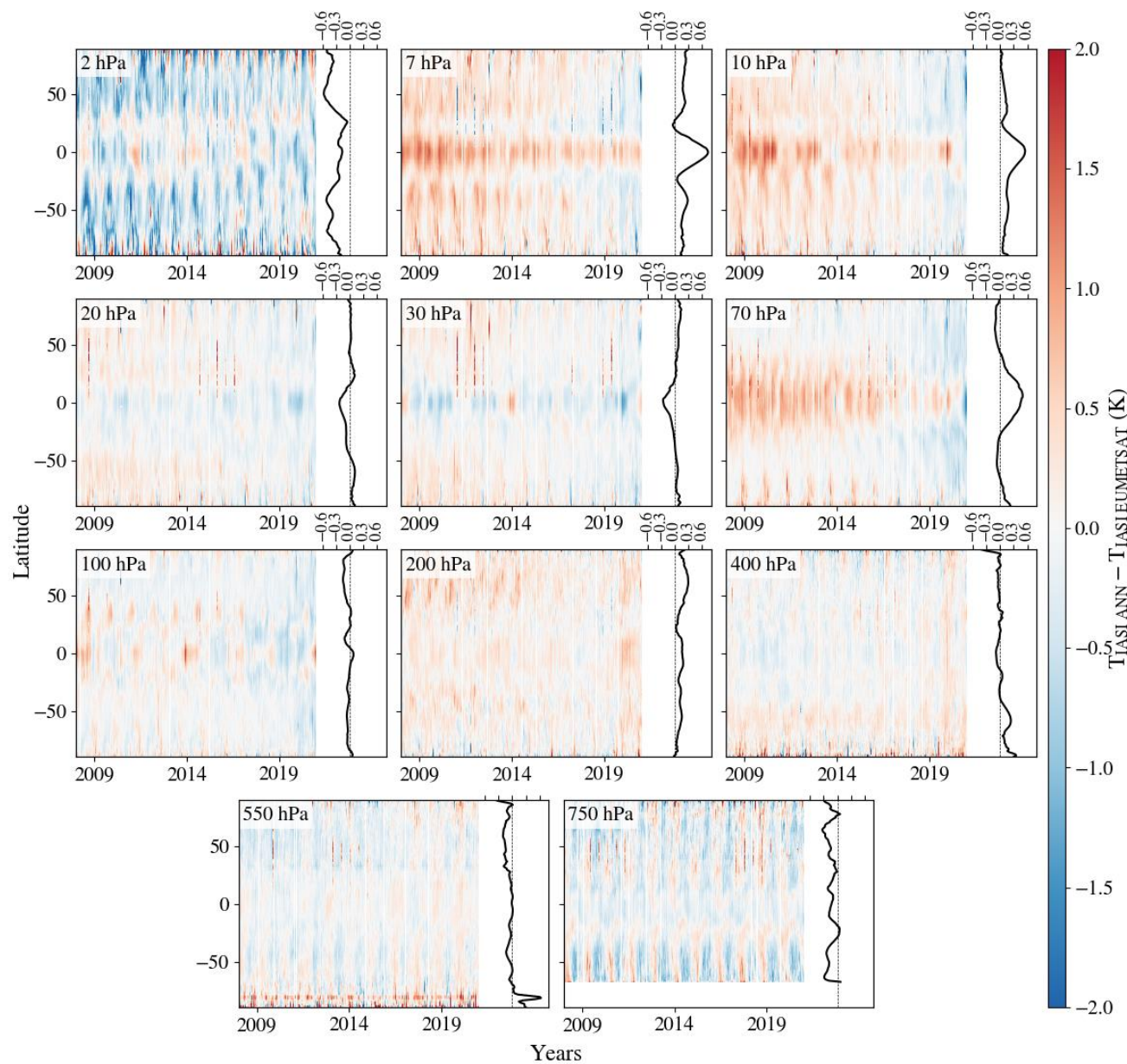
Figure 97: Daily zonal mean differences between IASI--ANN output and IASI EUMETSAT zonal mean temperature for the 11 pressure levels of the ANN. The red stripes seen in some panels are artefacts from the analysis and the do not reflect a physical phenomenon.
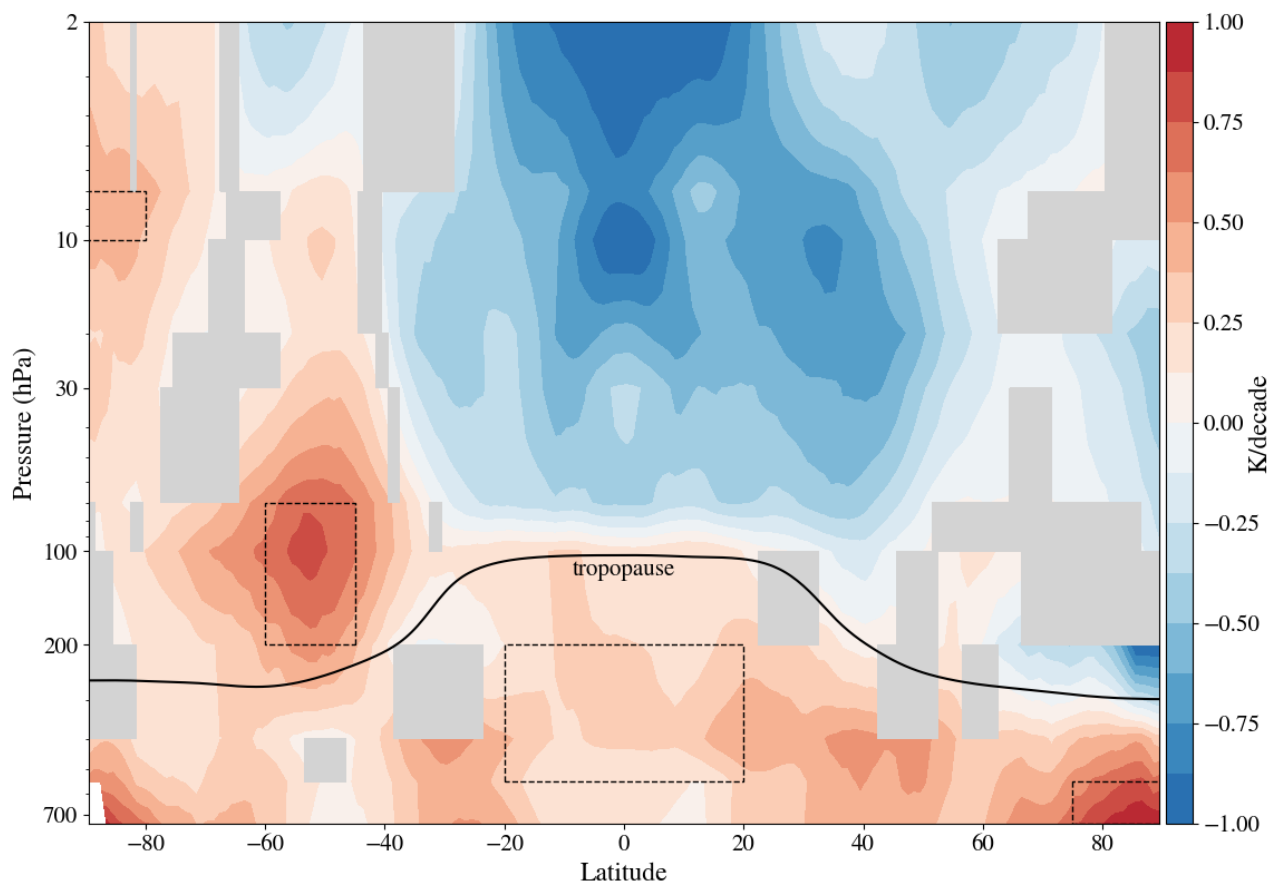
Figure 8: Zonal temperature trends for the period 2008-2020 computed with the outputs of the ANN. Grey areas correspond to trends that are not statistically significant. The dotted rectangles represent the regions for which the time series are shown in Figure 11
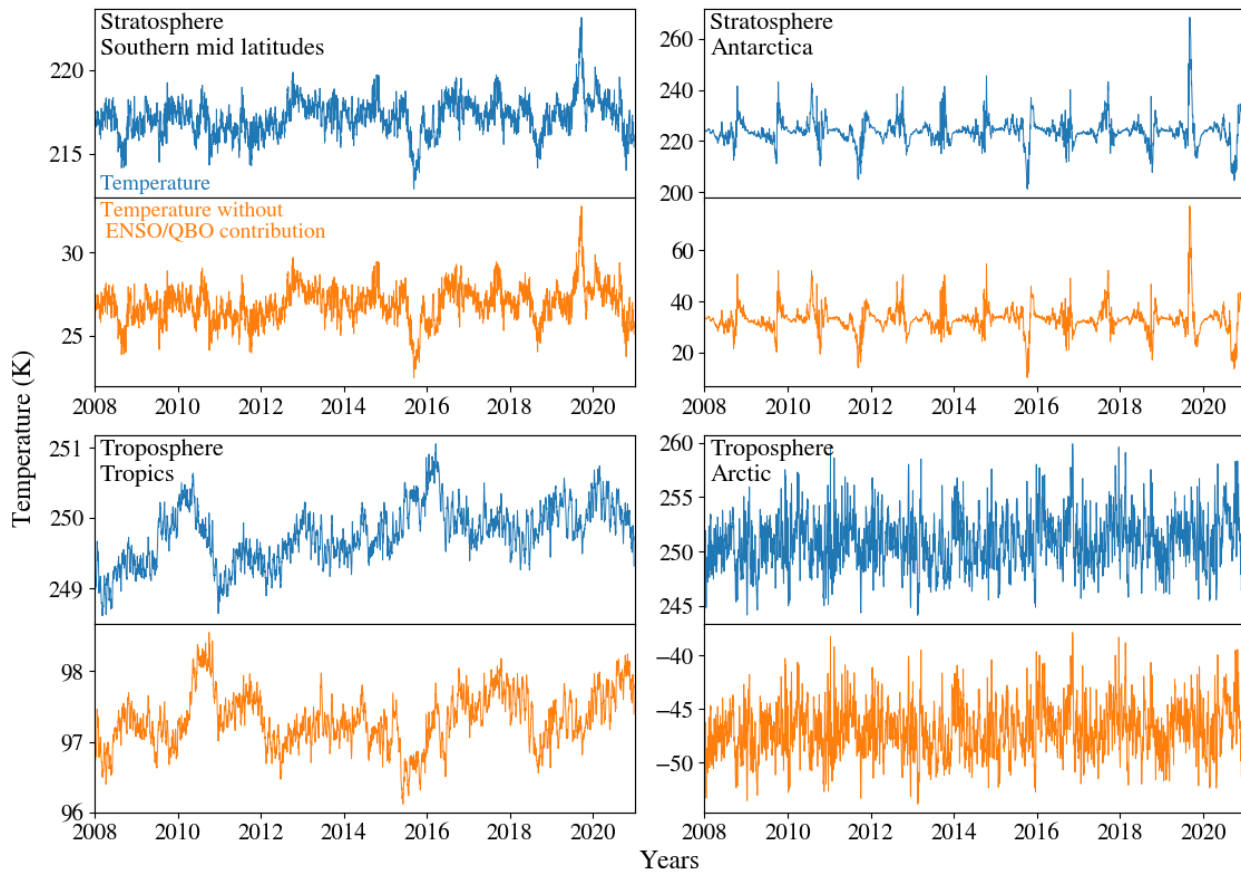
Figure 11: Times series of temperatures in the four rectangles of Figure 10 (blue) and time series without ENSO and QBO conttibutions (orange). The exact locations of the four regions are 45°S-60°S and 100-70 hPa for Stratosphere Southern mid latitudes, 80°S-90°S and 10-7 hPa for Antarctic stratosphere, 20°S-20°N and 550-200 hPa for Tropical troposphere, and 75°N-90°N and 750-550 hPa for Arctic troposphere.